Biomaterials Science

Volume 5
Number 5
March 2017
Pages 343-602

rsc.li/biomaterials-science

ISSN 2047-4849

PAPER
Soo Hyun Kim et al.
Biodegradable vascular stents with high tensile and
compressive strength, a novel strategy for applying
monofilaments via solid-state drawing and shaped-annealing
processes

ROYAL SOCIETY OF CHEMISTRY

European Society for Biomaterials

ROYAL SOCIETY OF CHEMISTRY

rsc.li/biomaterials-science

ARTICLE

On demand synthesis of calcium phosphate crystals in droplet micro-reactors of continuous operation

Konstantinos Tsachouridis[1], Ahlam Al Hadhrami[1], Antonios D. Anastasiou[1*]

In this work is demonstrated the use of droplet microreactors for the on-demand synthesis of three calcium phosphate minerals. In a simple three-inlet, flow focusing design, microdroplets serve as isolated reactors where crystals are formed under controlled conditions. Selective production of brushite, hydroxyapatite, or fluorapatite is achieved by modulating only the composition and the pH of a buffer stream without disturbing the flow regime and the continuous opeation of the system. Temperature and residence time have been proved key variables to control the properties of the resulted particles. Moving from 25 to 37 °C resulted in more crystaline material while by increasing residence time from 2 to 10 min bigger particles were obtained. Comparing with the standard batch synthesis, in microfluidics crystalisation crystals are less aggragated and smaller in size. During μ-LIF measurements it was confirmed that the formation of the crystals affects mixing quality within the droplets and this can be a field of improvement in order to get particles with more consistent properties. Overall this work, shows the potential of droplet microreactros as a versatile "factory-on-chip" toll for continuous production of biomaterials. Beyond calcium phosphates, the sama approach provides a scalable route to precision synthesis of multiphase and composite materials, enabling new frontiers in biomedical translation and advanced manufacturing.

1. Introduction

The synthesis of calcium phosphates (CaPs) has been a subject of intensive research, that is driven by the wide range of applications of these minerals in tissue engineering [1]. Their biocompatibility, regenerative potential and their chemical and structural similarity with the mineral of human hard tissues [2], make them ideal candidates for the fabrication of implants, scaffolds, bone cements and other medical devices [3]. Various synthesis methods for CaPs have been investigated in lab scale over the years as for example sol-gel synthesis [4] and hydrothermal methods [5] however, wet precipitation is the most well studied route due to its simplicity, low temperature and pressure, and easy translation to industrial production. One of its great advantages is that the mineral phase and the properties of the synthesised calcium phosphate crystals can be controlled by adjusting the conditions of the reaction as temperature, pH, residence time and Ca to P ratio [6]. For example, at acidic pH (4-6) formation of monocalcium and dicalcium phosphates (e.g. brushite) is favoured while at higher pH (>7) tricalcium phosphate and/or hydroxyapatite can be obtained [7]. On the other hand, temperature can be the means to control the crystallinity of the minerals and the characteristics of the final particles [2]. For large scale production, precipitation is taking place in batch, stirred tank reactors. Although the implementation of the

synthesis procedure is simple and the operating cost of these reactors is low, there are issues like low mixing efficiency and heterogenous concentration and temperature gradients that can affect the quality of the final product [8]. From process engineering point of view batch synthesis is more difficult to control while the start-stop nature of batch operation increases downtime and lowers overall productivity of the unit.

A potential solution to improve the properties of the synthesised CaPs and the efficiency of the production is the use of mili/micro – fluidic reactors of continuous operation. The small volumes of fluids involved in microfluidics offer good regulation of operating conditions like reactant concentrations, temperature gradients and mass transfer rates [9], [10]. As it is documented in literature for various nanoparticle systems, the synthesis in microfluidics results into crystals with narrow size distributions and well-defined properties [11], [12]. Amongst the advantages of microfluidics is also the potential of straightforward scaling up by operating continuously multiple parallel microreactors [13], [14], [15]. Various reactor designs have been proposed over the years for the synthesis of nanoparticles including CaPs [6], [11]. A modular oscillatory flow reactor was extensively investigated by Veiga et al [16] were operating parameters like oscillation amplitude, residence time and temperature have been investigated to identify how the properties of the obtained CaPs can be controlled. This type of reactor was indicated as a potential platform to satisfy the needs of industrial production. Droplet microreactors are also a viable option for the synthesis of crystals with key advantages the well-controlled volume of reaction (volume of the droplet) and the reduced fouling [17]. In

Lab of Complex Fluids and Microfluidics, Department of Chemical Engineering, University of Manchester, Manchester, UK, M1 3AL
*Antonios.anastasiou@manchester.ac.uk

the work of Galván-Chacón, et al [18] such a devise was utilised to produce a variety of CaP based biomaterials (e.g. hydroxyapatite) and the formation of spherical micro-particles of controlled size and porosity was demonstrated. Tsachouridis et al, [19] assessed three types of droplet-microreactors for the continuous production of metal oxide and CaP nanoparticles. A three-inlet, flow focusing design was identified as the most appropriate for long-term operation. The key feature of this design is a buffer, aqueous stream that keeps the raw materials separated at the droplet formation point preventing the fouling of the crystals and the blocking of the channels. This buffer stream can be also used to tune the reaction conditions within the droplets. Motivated by this, the present work aims to explore how the phase and the characteristics of the CaP crystals can be controlled during the continuous operation of the microreactor. The main objective is to demonstrate the on-demand synthesis of three well known CaP phases by only changing the composition of the buffer stream without disturbing the flow pattern and the general operation of the microreactor. Amongst CaPs, hydroxyapatite [HAP: $Ca_{10}(PO_4)_6(OH)_2$], brushite (DCPD: $CaHPO_4 \cdot 2H_2O$) and fluorapatite (FAP: $Ca_5(PO_4)_3F$) are three of the most well documented with wide range of applications in orthopaedics and dentistry [7] and for this reason became the focus of this study. Brushite crystals are formed at pH < 5.5 and typically have a flake-like shape and size, reaching up to 40 microns [20]. HaP crystals on the other hand are typically formed at alkaline environment, and they have a needle-like shape [6]. Fluorapatite is formed at the same conditions as HaP and in the presence of F$^-$ ions that substitute OH$^-$ in the crystal lattice [21]. In the first stage of our study, droplet formation experiments have been conducted to identify the appropriate operating conditions of the microreactor. To confirm the phase of the obtained minerals characterisation techniques like X-ray diffraction and transmission electron microscopy have been utilised. A comparison between the materials from the microfluidics synthesis and the standard batch process was made to understand the effect of the different synthesis variables.

2. Materials and methods

2.1 Fabrication of the microreactors and experimental setup

A commercial CAD software (Autodesk Fusion 360) was used to design the microfluidic channels (**Figure 1a**), which were then fabricated in a high-resolution, resin 3D printer (Sonic Mini 8K) using a transparent, low-viscosity resin (BV007A, Creative CADworks) with absorbance at 390 nm. A thickness of 30 μm was selected for each printing layer, and the exposure time was set to 1.8 s. After printing, the microchannels were cleaned with isopropanol (IPA) and then rinsed with water to remove any residual resin. The devices were then cured for 2 min under UV light to complete the polymerization of the resin. The open microchannels (**Figure 1b**) were sealed with Kapton tape (Tesa 51408) and were fixed on a chip holder, between two metallic plates.

For the microfluidics synthesis, based on our previous works [19] a concentration of 0.04 M was selected for the precursor (R1; $Ca(NO_3)_2 \cdot 4H_2O$, Sigma-Aldrich, CAS:13477-34-4) and precipitation

agent (R2; $Na_2HPO_4 \cdot 2H_2O$ (Sigma-Aldrich, CAS: 7558-79-4)). A high-viscosity silicone oil (100 cSt at 25 °C, Sigma-Aldrich, CAS: 63148-62-9) (O1) was the continuous phase during all the experiments. High accuracy syringe pumps (NE-1000 Syringe Pump) were used for the circulation of liquids and control of the flow rates. To regulate the residence time, tubing of appropriate length and inner diameter of 1 mm was connected at the exit of the microreactor. The microreactor and the tubing were placed in a water bath (Cole-Parmer WB-400) to control temperature. The droplets were collected in a beaker (Figure 2), and the separation of the three-phase mixture (oil-water-particles) was achieved in a centrifuge (FastGene® High-Speed Mini Centrifuge, Cat.No.: NG003) at 11,000 rpm. The particles were collected, washed, and then placed in a freezer at -25 °C overnight. Drying was performed in a freeze dryer (VirTis Benchtop pro) operating at 150 mTorr and -90 °C.
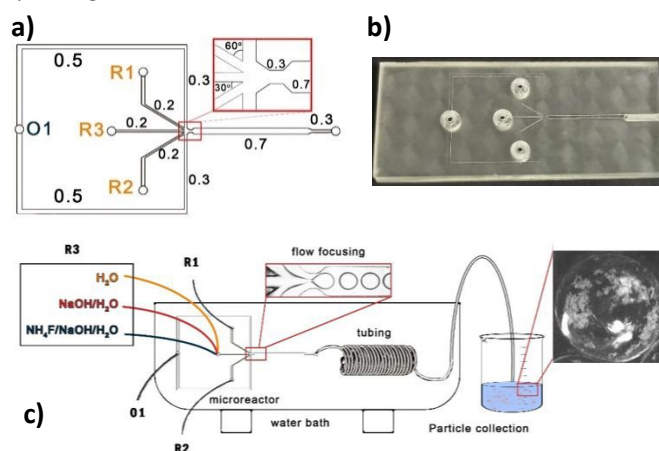

Figure 1. Design of the microreactor and experimental setup**. a)** Microfluidic channel geometry; **b)** Protype microreactor; **c)** Experimental setup for microfluidic synthesis.

The synthesized materials are listed in **Table 1.** For brushite synthesis (R3 is H_2O solution) at 25 °C, residence times (RTs) in the microreactor (including the outlet piping) of 2 min (MBr1) and 10 min (MBr2) were used and at 37 °C RTs of 2 min (MBr3) and 10 min (MBr4). The same protocol was used for the microfluidic HaP (MHaP) synthesis (R3 is $NaOH/H_2O$ solution), whereas for the microfluidic fluorapatite (MFaP1) R3 is NH_4F (Sigma-Aldrich, 12125-01-8), $NaOH/H_2O$), only a RT of 2 min at 37 °C was explored.

Table 1: Synthesised materials and reaction conditions.

Mineral	Method	Code	T (°C)	RT (min)
Brushite	Batch	BBr	37	120
	Microfluidic (R3:H_2O)	MBr1	25	2
		MBr2	25	10
		MBr3	37	2
		MBr4	37	10
HAP	Batch	BHaP	37	120
	Microfluidic (R3:$NaOH/H_2O$)	MHaP1	25	2
		MHaP2	25	10
		MHaP3	37	2
		MHaP4	37	10
FAP	Batch	BFaP	37	120
	Microfluidic			

(R3:NH₄F/NaOH/H₂O)	MFaP1	37	2

2.2 Batch synthesis of CaPs

For the batch synthesis of Batch brushite (BBr), a 0.1 M $Ca(NO_3)_2 \cdot 4H_2O$ aqueous solution (200 mL) was heated to 37 °C, and then a 0.1 M $(NH_4)_3PO_4$ solution (200 mL) was added dropwise. The final mixture was left under continuous stirring at 37 °C for 2 h, then left to settle for 2 h to allow precipitation. During these steps, the top of the beaker was sealed with aluminum foil to exclude CO_2 ingress into the phosphate mineral solution. The formed brushite crystals were washed several times with distilled water, placed in the freezer at -20 °C overnight and freeze-dried. For the synthesis of batch hydroxyapatite (BHaP), the same procedure was followed, but NaOH solution was also added dropwise simultaneously with the addition of the $(NH_4)_3PO_4$ solution to maintain a pH above 10, while for the synthesis of batch Fluorapatite (BFaP), a $NH_4F/NaOH$ solution was used instead.

2.3 Materials' characterisation

TEM images of calcium phosphates were obtained using a FEI Tecnai G 20 microscope at an accelerating voltage of 200 kV. TEM samples were prepared by obtaining a suspension from the particle powder in ethanol, followed by dropping it on a carbon-coated grid and drying for 2 h.

The XRD measurements were conducted on a PANalytical X'Pert Pro that has a θ:θ geometry. The X-ray source is a copper sealed tube target producing Cu kα and kβ emission lines from a generator operating at 40 kV and 40 mA. An incident beam Soller slit of 0.04 rad, 2° fixed antiscatter slit, an incident beam mask of 10 mm, a programable automated divergence slit giving a constant illuminated length of 10.0 mm, and a Soller slit of 0.04 rad were used. Data were collected from 5 to 85° using a step size of 0.02 deg. and time per step 1.2 s. The datasets were analyzed using X'Pert Highscore Plus [22] and the International Centre for Diffraction Data (ICDD), using reference patterns for brushite (PDF 09-0077), hydroxyapatite (PDF 09-0432) and fluorapatite (PDF 15-0876).

The morphology of the calcium phosphate samples was examined using a FEI Quanta 650 microscope under high vacuum and an accelerating voltage of 10 kV. The samples were fixed on aluminum stubs and coated with a 6 nm Au/Pd (80:20) layer using a Quorum coater.

2.4 Droplet characterisation and mixing experiments

For identifying the appropriate operating conditions of the microreactor droplet characterisation experiments have been conducted. All experiments were monitored using a high-speed camera (AOS S-MIZE) and an inverted microscope (KERN OCM-161). Videos with a frame rate of 1500 fps were captured and frame-by-frame analysis was performed to determine the droplet size and formation rate.

Mixing withing the droplets was investigated for a non-reactive system with all inlets containing deionised water, and a reactive system where brushite precipitated from calcium nitrate and ammonium phosphate solutions. Measurements were obtained at four positions—droplet formation, immediately after inlet merging (6 mm), mid-channel (15 mm), and near the outlet (30 mm). Rhodamine B dye was added to one aqueous inlet to perform Micro-Laser Induced Fluorescence (μ-LIF) with a system comprising from a Nikon Eclipse Te200 inverted microscope, a PCO Panda 26 DS camera and a Pulsed laser (LD-PS/5, Optolution). Image acquisition and processing was achieved with the use PIVlab on MATLAB2021a.

3. Results and discussion

3.1 Droplet formation and flow conditions for CaP synthesis

Droplet formation experiments have been conducted for understanding how droplet size is affected by parameters such as viscosity of the continuous phase and flow rate ratio and for identifying the appropriate flow conditions for the synthesis experiments. As shown in **Figure 2a**, the microreactor features a triangular merging region where the three dispersed phase streams converge and droplets are formed. After the first merging of the aqueous streams the droplet formation is stabilised to the dripping regime for a wide range of flow rates (no jetting was observed for the studied flow rates). When the two oils with viscosity of 100 cSt and 10 cSt were tested, it was found that for the same flow conditions the high viscosity oil consistently resulted in slightly smaller droplets. This is reasonable considering that as viscosity increases the viscous forces become higher and overcome interfacial tension (increase of Capillary number) [23]. The other key difference between the two oils is that for 10 cSt, pronounced merging of droplets was observed after their formation and during their flow in the microchannel and particularly at the outlet of the microreactor.

Flow rate ratio (Q_c/Q_d) is the variable with the strongest effect on droplet size. For the 100 cSt oil, increasing Q_c/Q_d from 0.1 to 0.5 results in a dramatic reduction of the average diameter from 1.2 mm to 0.6 mm. The minimum droplet size is achieved for Q_c/Q_d =2, and further increase has practically no effect on the diameter. The experimental results were compared with a correlation proposed in literature for predicting droplet size [24]; scaling law is expressed as

$$D = w + w \cdot a \frac{Q_d}{Q_c} \quad (1)$$

where D is droplet diameter, w is the channel width and Q_d/Q_c is the dispersed-to-continuous phase flow rate ratio and α is an order one constant that depends on the geometry of the microreactor [24]. This model relates droplet size to the interplay between geometric confinement and flow rate of continuous and dispersed phase. As shown in **Figure 2b**, the model exhibits strong agreement with experimental data, particularly for Q_c/Q_d > 0.5, where flow is dominated by dripping mechanisms. In this regime, the balance of interfacial and viscous forces is well captured by the scaling law. At larger droplet sizes, the model tends to overpredict, with the greatest deviation observed at 1.17 mm measured versus 2.99 mm predicted. Despite this, the model achieved a high correlation (R^2 = 0.787) and an average absolute error of ~13%, confirming its suitability for rapid droplet size estimation under controlled flow conditions.

Based on the results from the flow experiments, Q_c/Q_d =1.73 and oil viscosity of 100 cSt were identified as the appropriate

ARTICLE

operating conditions and were kept the same for all the synthesis experiments having in mind both the size of the droplets but also the total flow rate of the oil. To maintain isolated reaction environment the use of high-viscosity oil was preferred since it stabilizes droplet boundaries reducing the chances of merging.
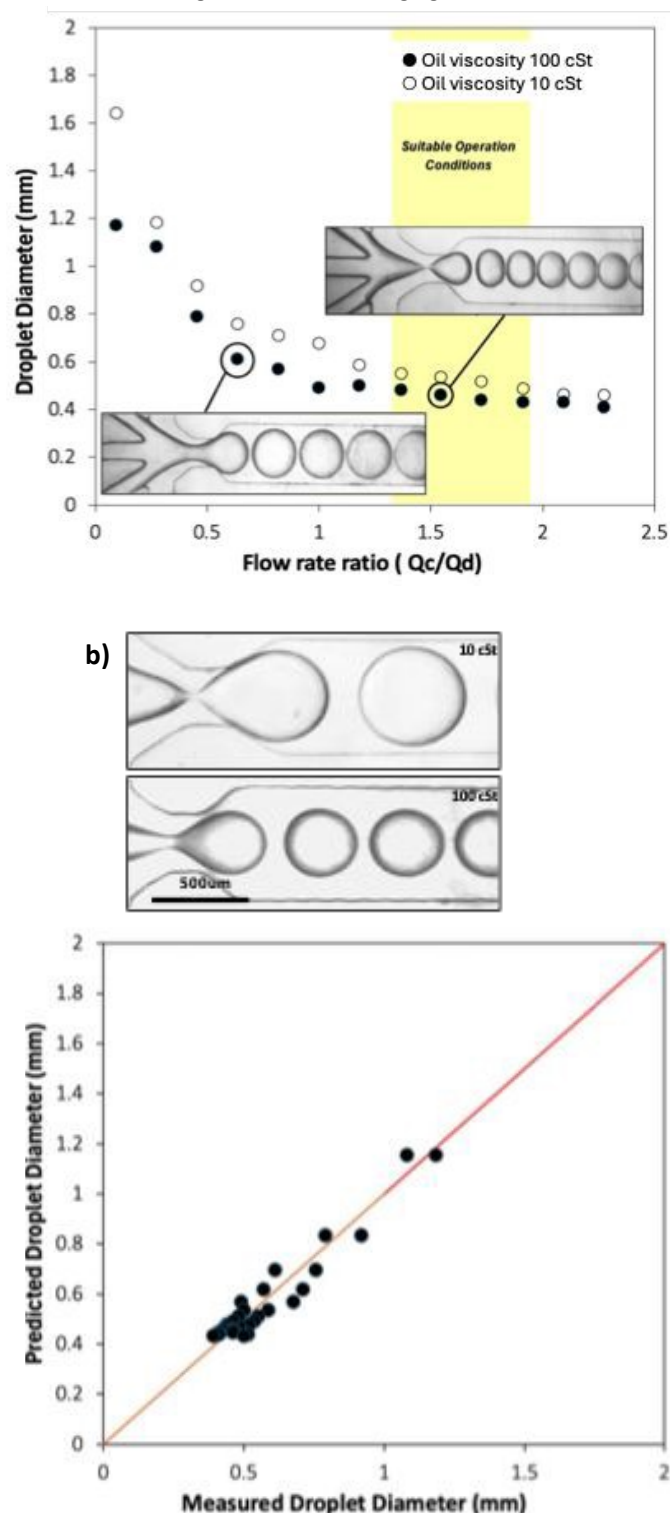

Figure 2: Droplet formation experiments in the microreactor; a) Droplet diameter as a function of the flow rate ratio (Qc/Qd) and identification of appropriate operating conditions; b) Indicative droplet size at Qc/Qd = 1.0 for oils 10 and 100 cSt, c) Comparison of experimentally measured droplet sizes with predictions from literature-based scaling law.

3.2 CaP synthesis in microreactors

During the first synthesis it was important to monitor the flow of the droplets and to verify that there is no merging throughout the flow path (**Figure 3**). As it is depicted in **Figure 3a** and **3b**, the droplets maintain the same shape and size from the formation point to the entrance of the final tubing. As shown in **Figure 4b**, droplets progressively lose transparency, indicating the onset of nucleation. The emergence of solid-phase material within the droplets confirms that crystal formation begins during transit through the channel and continues into the collection reservoir. After collection, the droplets were examined under the microscope; **Figures 4c–e** display droplets after 10 min of synthesis time. Fine particulate material is visible inside the aqueous phase, confirming the successful in-droplet precipitation of CaPs. For all the synthesis experiments it was confirmed that the droplet size is unaffected from the occurring reaction and matched the findings from the initial hydrodynamic experiments.
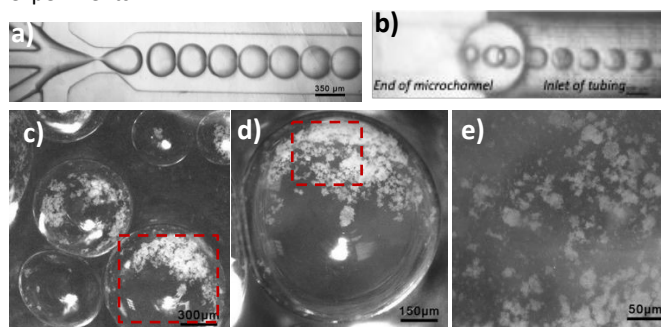

Figure 3. Observation of the droplets during brushite synthesis; a) droplets at the merging chamber; b) droplets exiting the MR and entering the microtubing; c-e) droplets in the collection beaker and crystals inside the droplets after 10 min of synthesis.

Brushite Synthesis

Brushite was synthesised in the microreactor for temperatures 25 °C and 37 °C and residence times 2 and 10 min. In the SEM and TEM images (**Figure 4**), distinct morphological differences were observed between the batch and microfluidic synthesis. The materials obtained from the first (**Figure 4. 1a, 2a**) exhibited large-area flake-like crystals averaging slightly over 10 µm in length, indicating a less controlled growth environment. In contrast, the microfluidic samples exhibited a progression in crystal development as both the temperature and the residence time were increased. At 25 °C for 2 min (Figure 4.1b, 2b), the flakes were underdeveloped, averaging 1.5 µm in length, indicating limited growth and potentially rapid nucleation under short exposure to the reagents. Extending the reaction time to 10 min at 25°C (**Figure 4.1c, 2c**) led to a slight increase in crystal size, with average dimensions of 2 µm in length. At a higher temperature of 37 °C for 2 min (**Figure 4.1d, 2d**), the crystals were more developed, with an average length of 4 µm, highlighting the influence of increased temperature on accelerating crystal maturation. The most well-developed flakes were observed at 37 °C for 10 min residence time (**Figure 4.1e, 2e**), where the crystals reached an average of 7 µm in length and up to 3 µm in width. These results suggest that both high temperature and long exposure times contribute to the formation of mature and well-

structured crystals. The correlation between synthesis conditions and crystal morphology suggests that microfluidic synthesis provides greater control over the size and development of brushite crystals than batch synthesis. Also, it is clear that the formation of the crystals is taking place much faster in the microreactor since the materials for 10 min residence time are comparable to the batch synthesis where the reactants remain in contact longer and the precipitation lasts for several hours.
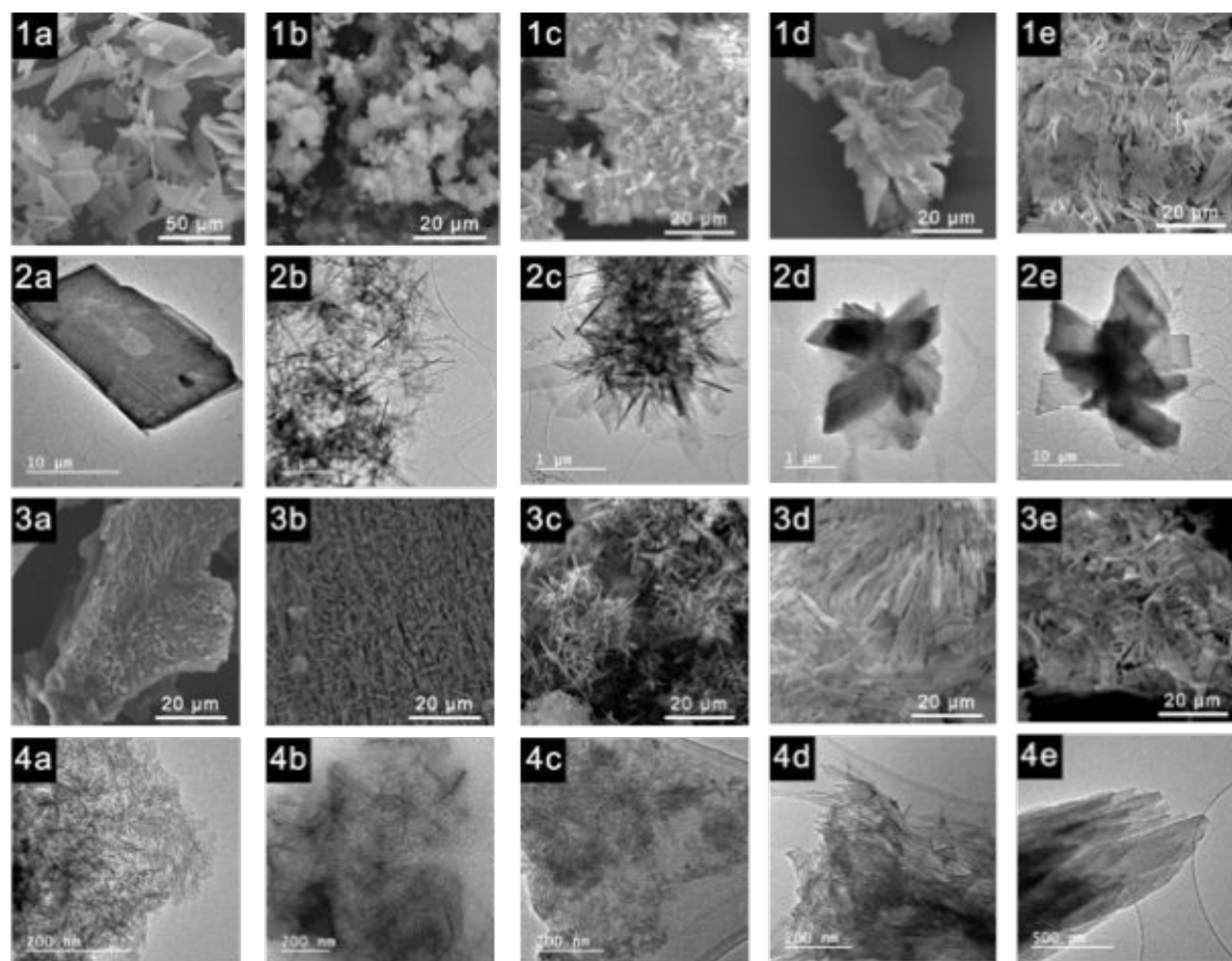

Figure 4: Scanning and transmission electron microscopy for all the synthesised materials**. First row SEM images of brushite: 1a) BBr; 1b) MBr1; 1c) MBr2; 1d) MBr3; 1e) MBr4. Second row, TEM images of brushite: 2a) BBr; 2b) MBr1; 2c) MBr2; 2d) MBr3; 2e) MBr4. Third row, SEM images of hydroxyapatite: 3a) BHaP; 3b) MHaP1; 3c) MHaP2; 3d) MHaP3; 3e) MHaP4. Fourth row TEM images of hydroxyapatite: 4a) BHaP; 4b) MHaP1; 4c) MHaP2; 4d) MHaP3; 4e) MHaP4.

In **Figure 4a**, the XRD analysis verified the similarities of the materials obtained from the batch and microfluidic synthesis indicating in all cases brushite as the dominant phase. The pattern for BBr shows a highly crystalline material (sharp, clear peaks) with all the characteristic peaks of brushite (PDF 09-0077). The microfluidic synthesis at 25 °C (MBR1 and MBR2) resulted in less crystalline material and the characteristic peak of brushite at 11.5° has low relative intensity indicating underdeveloped crystals. The effect of residence time for this temperature seems to be negligible since the two patterns for 2 and 10 min are similar. When temperature is increased to 37 °C the resulted crystals give patterns closer to the ones of the batch synthesis. The materials seem to be more crystalline comparing to MBR1 and MBR2 and the peak at 11.5° is of considerable height. It is worth mentioning that the relative intensity of this peak is not only a matter of the crystal structure of the material but is also affected by the geometry of the crystals. Brushite's flake like crystals tend to align during sample preparation, producing a strong texture effect that enhances reflections parallel to the (0 1 0) plane, with most characteristic example the 11.6° peak [25]. This alignment arises from the intrinsic anisotropy of brushite, where the (0 1 0) plane forms the main basal face and growth along (0 1 0) is comparatively slow. The lower intensity of this reflection in the 25 °C samples (MBr1–MBr2) indicates less developed flake orientation, while at 37 °C (MBr3–MBr4) the stronger (0 1 0) peak confirms more complete development of these faces, consistent with the larger and well-defined crystals seen in SEM. Overall, it is evident that during the microfluidic synthesis, temperature is the variable that affects the most the crystal structured of the material. On the

other hand, the effect of residence time for brushite is more apparent to the size of the crystals and not the crystallinity or the resulted mineral phases.

Synthesis of hydroxyapatite

To switch from brushite to hydroxyapatite, NaOH is introduced in the buffer stream aiming to alkaline conditions (pH > 8.5) within the droplets. The SEM and TEM images of the HAP crystals revealed differences in morphology between the synthesis methods. The batch obtained material (**Figure 4.3a, 4a**) appears as highly aggregated rod-like structures, with individual crystals measuring less than 200 nm in length. This aggregation may be due to the rapid nucleation and limited growth control of the batch synthesis process, resulting in densely packed nanostructures. On the other hand, the microfluidic samples displayed better defined crystal formations, with a clear trend toward increased growth as both temperature and residence time were increased.

At 25 °C for 2 min (**Figure 4.3b, 4b**), the HAP crystals formed underdeveloped needles, but with less aggregation compared to the batch method, indicating some degree of separation. Extending the reaction time to 10 min at the same temperature (**Figure 4.3c, 4c**) led to more developed and bigger in size, needle-like structures. At 37 °C for 2 min (**Figure 4.3d, 4d**), the crystals shifted to more well-defined rod-like shapes, reaching a few microns in size. These rods showed slight aggregation, suggesting that although higher temperatures promoted growth, there was still some tendency for the crystals to cluster. Finally, at 37 °C for 10 min (**Figure 4.3e, 4e**), the crystals exhibited rod and flake-like structures that were highly aggregated, with individual crystals still in the microns range, which again suggests prolonged contact time in the droplet promotes crystal interaction and clustering. This increase in aggregation is directly linked to the larger crystal sizes formed under these conditions.

The difference in morphology observed between brushite and hydroxyapatite, results from the inherent crystal structures of the two phases. Brushite grows as thin plates because its lattice favours expansion of broad, flat surfaces, whereas hydroxyapatite grows as needles and rods due to its strong axial growth along the crystallographic c-direction. These phase-specific growth behaviours, well established in the work of LeGeros [26], fully explain the transition from flake-like brushite to rod-like hydroxyapatite under otherwise similar microfluidic conditions.

Overall, these observations show that the microfluidic environment provides tighter control over crystal size and morphology compared to batch synthesis, although longer reaction times and higher temperatures can lead to increased aggregation, particularly in the case of the hydroxyapatite crystals. The ability to tune these parameters is critical for optimizing the material's structural properties for specific applications.
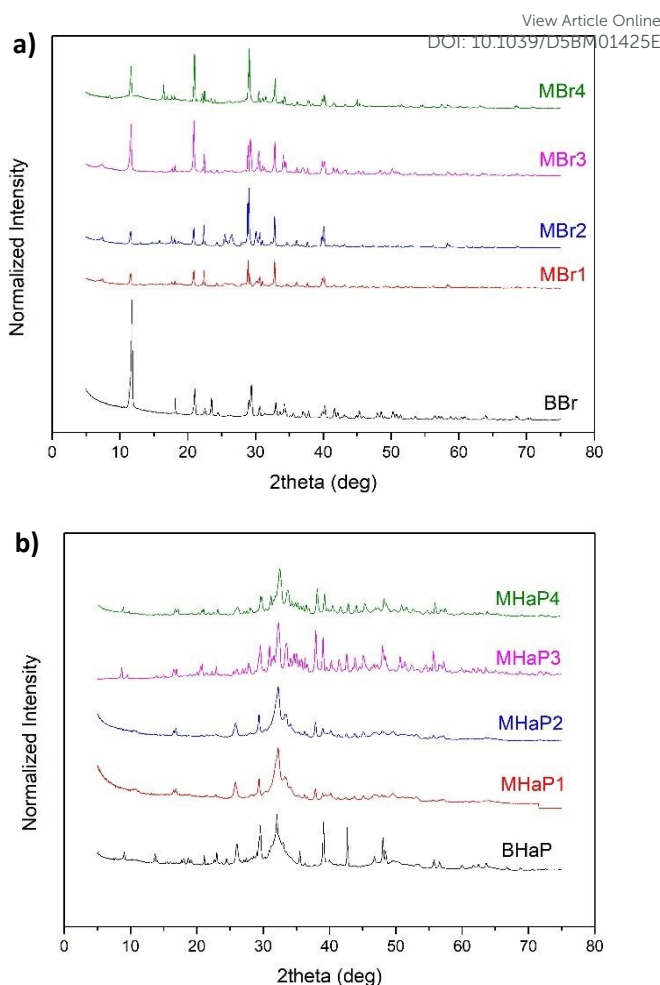

Figure 5. Comparison of X-ray diffraction patterns for the materials obtained from the different microfluidic experiments with the batch synthesis; a) XRD graph of Brushite crystals. b) XRD graph of Hydroxyapatite crystals.

The XRD results (**Figure 5b**) confirmed that in all samples, hydroxyapatite was the dominant phase since the characteristic peaks at 26° and the multiple peaks between 32° and 33° were identified. The batch synthesised material (BHaP) shows the narrowest, most intense peaks, indicating the highest crystallinity. Prolonged residence time at mild temperature allows diffusion-limited growth and defect annealing. Microfluidic synthesis at 25 °C with a short residence time (MHaP1) yielded broader peaks, reflecting smaller crystallite sizes and higher microstrain. Extending the residence time to 10 min at 25 °C (MHaP2) resulted in slightly narrower peaks, indicating growth and partial defect annealing. Increasing the synthesis temperature to 37 °C enhanced crystallinity even at short residence times. MHaP3 displayed sharper peaks than MHaP1, demonstrating the role of temperature in accelerating crystal growth. The combination of higher temperature and extended residence time (MHaP4) produced the most crystalline microfluidic sample, approaching the peak sharpness and intensity of BHaP.

The reflection at ~26° (0 0 2), associated with crystal growth along the c-axis, is more pronounced in the batch material (BHaP) and in

the 25 °C samples (MHaP1–MHaP2), indicating stronger alignment along this direction at lower temperature. In contrast, the 37 °C runs (MHaP3–MHaP4) exhibit a broader and less intense (0 0 2) peak but clearer separation of the reflections between 32° and 33° [(2 1 1), (1 1 2), (3 0 0)], suggesting higher overall crystallinity and reduced texture. This behaviour implies that increasing temperature and residence time improves lattice ordering and peak resolution but weakens the preferred c-axis orientation, which is consistent with the morphological transition from slender needles at 25 °C to thicker, more isotropic rods at 37 °C observed in TEM.

Fluorapatite synthesis

The transition from HAP to Fluorapatite (FaP) was achieved when F⁻ ions were introduced to the buffer stream. The obtained crystals were similar with what was achieved in the batch synthesis since in both cases small rectangular particles with smooth edges ranging from 20 nm to 100 nm were identified. Compared with the batch process (**Figure 6a**), the microfluidic particles (MFaPs) imaged by TEM (**Figure 6b**) were generally smaller and slightly less aggregated. Elemental analysis by STEM–EDS confirmed the successful formation of fluorapatite. The EDS spectrum (**Figure 6c**) identified characteristic peaks for calcium (Ca), phosphorus (P), oxygen (O), and fluorine (F), in agreement with the expected FaP stoichiometry. Mapping of the elemental distribution across selected MFaP aggregates (**Figure 6d–g**) showed a uniform spatial distribution of Calcium (Ca), Phosphorous (P), and Fluoride (F), supporting the incorporation of fluoride within the apatite lattice.
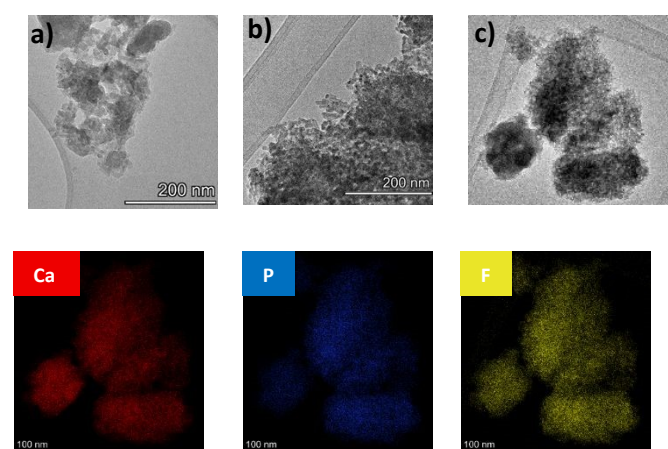

Figure 6. Transmission electron microscopy for the fluorapatite; a) TEM batch FaP, b) TEM microfluidic FaP, c) EDS spectrum and elemental analysis of MFaP, d) TEM MFaP image used for EDS mapping, e-g elemental maps for Ca, P and F, respectively.

3.3 Mixing within the droplets in reactive and non-reactive conditions

The mixing within the droplets was investigated for a reactive and a non-reactive system. For the first scenario the synthesis of brushite at 25 °C was selected. Fluorescence imaging revealed sharp dye boundaries at the merging point for both cases, confirming effective separation of aqueous streams and absence of premixing before droplet formation. Immediately downstream, both systems

exhibited a central dye-free region flanked by fluorescent zones, indicating limited initial mixing. The non-reactive system exhibited smoother radial dye diffusion, suggesting a tendency toward more homogeneous mixing, although the persistent central dark zone indicated incomplete homogenization at 15 mm distance from the droplet formation point. In contrast, the reactive system displayed pronounced internal heterogeneities characterised by irregular bright and dark patches, indicative of localised compositional variations and disrupted internal circulation likely caused by the ongoing chemical reactions and the formation of the brushite crystals. At 30 mm, droplets in the non-reactive system present only a very narrow central dark zone surrounded by diffuse fluorescence, confirming the high degree of mixing. The droplets with reaction occurring on the other hand, exhibited complex internal structures with scattered bright and dark regions, reflecting localised concentration differences and disrupted flow due to reaction-induced changes such as variations in viscosity, interfacial tension, particle formation, or phase separation. Overall, mixing was smoother and more uniform in the non-reactive system, though neither system achieved complete homogenization within the observed timeframe. The reactive system's internal heterogeneities highlight the significant influence of chemical reactions on droplet mixing and flow dynamics. This behavior can be explained if we consider the brushite crystals and the crystal clusters that appear in the reactive system (Figure 5-2b). Both can behave as moving obstacles that distort streamlines, split the two canonical toroidal vortices that are expected to appear in the microdroplets, and create stagnant pockets where diffusion dominates the mixing. The lack of fluid movement within the droplet can lead to bigger crystal clusters and regions with higher concentration gradients which influences subsequent crystal growth. Although this effect was not quantified here, it is consistent with the μ-LIF observations and explains the poorer mixing seen under reactive conditions.

Even though nucleation initiates shortly after the reagents first meet, the subsequent evolution of the crystals remains strongly dependent on the internal concentration and pH fields, which are governed by mixing. The μ-LIF results demonstrate that reactive droplets maintain persistent compositional gradients, meaning that different regions inside the same droplet undergo different nucleation densities and experience unequal growth environments. Improving mixing reduces these gradients and produces a more uniform supersaturation field, which in turn supports a more synchronised nucleation process and more homogeneous crystal growth despite the short nucleation timescale.
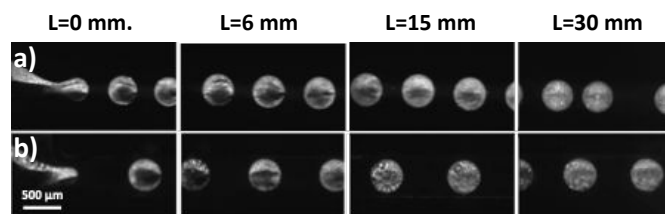

Figure 7: μ-LIF images showing internal mixing within droplets at the merging point (L=0 mm), post-merging (L=6 mm), mid-channel (L=15 mm), and channel outlet (L=30 mm) for; **a)** a non-reactive system; **b)** brushite synthesis at 25 °C.

4. Conclusions

ARTICLE

This study demonstrates the use of a droplet microfluidic platform as a versatile and controllable route for the on-demand synthesis of calcium phosphate minerals. By modulating only, the composition of a buffer stream, synthesis of different mineral phases i.e. brushite, hydroxyapatite, and fluorapatite can be achieved without disturbing the droplet flow pattern and the continuous operation of the system. Temperature found to be the means to control the crystallinity of the material while, residence time had a significant effect on the size of the crystals both for brushite and hydroxyapatite. Compared to batch precipitation, microfluidic synthesis yielded smaller particles with reduced aggregation while providing enhanced control over crystal morphology and orientation, owing to the highly stable and spatially confined reaction environment that enables uniform nucleation and directional crystal growth. This acceleration was achieved without compromising phase purity, as confirmed by XRD and elemental analysis. In microfluidics crystals comparable to those of the batch synthesis are obtained in much shorter times. On the other hand, there wasn't any proof of particles with consistent properties from the microfluidic synthesis. The μ-LIF measurements revealed that chemical reactions and the formation of crystals significantly alter droplet mixing patterns, which in turn influence particle uniformity and crystallinity. This disruption in the flow profile within the droplet is reasonable, particularly for the case of systems like brushite where the size of the crystals is comparable to the size of the droplets. Consequently, improving mixing conditions by adding appropriate geometrical features to microreactor design (e.g. stenosis and curvatures) to manipulate droplet hydrodynamics is critical for obtaining crystals of more consistent properties.

Building on the results of this study, future research should focus on integrating real-time monitoring techniques, such as in-line spectroscopy and advanced imaging, to further refine process control and improve reproducibility. Additionally, expanding the microfluidic approach to multi-phase material synthesis, including composite biomaterials, could offer new avenues for next-generation biomedical applications. Finally, collaboration with industrial partners to scale up microfluidic-based CaP production could bridge the gap between laboratory-scale research and commercial application, solidifying the role of microfluidics as a game-changing technology in biomaterial synthesis.

Acknowledgements

References

1. Anastasiou, A.D., et al., *Antibacterial properties and regenerative potential of Sr2+ and Ce3+ doped fluorapatites; a potential solution for peri-implantitis.* Scientific Reports, 2019. **9**(1): p. 14469.
2. Dorozhkin, S.V. *Nanodimensional and Nanocrystalline Apatites and Other Calcium Orthophosphates in Biomedical Engineering, Biology and Medicine.* Materials, 2009. **2**, 1975-2045 DOI: 10.3390/ma2041975.
3. Chen, X., et al., *Calcium Phosphate-Based Nanomaterials: Preparation, Multifunction, and Application for Bone Tissue Engineering.* Molecules, 2023. **28**(12): p. 4790.
4. Ishikawa, K., E. Garskaite, and A. Kareiva, *Sol–gel synthesis of calcium phosphate-based biomaterials—A review of environmentally benign, simple, and effective synthesis routes.* Journal of Sol-Gel Science and Technology, 2020. **94**(3): p. 551-572.

5. Chaudhry, A.A., et al., *Synthesis and characterisation of magnesium substituted calcium phosphate bioceramic nanoparticles made via continuous hydrothermal flow synthesis.* Journal of Materials Chemistry, 2008. **18**(48): p. 5900-5908.
6. Lin, K., C. Wu, and J. Chang, *Advances in synthesis of calcium phosphate crystals with controlled size and shape.* Acta Biomater, 2014. **10**(10): p. 4071-102.
7. Eliaz, N. and N. Metoki, *Calcium Phosphate Bioceramics: A Review of Their History, Structure, Properties, Coating Technologies and Biomedical Applications.* Materials (Basel), 2017. **10**(4).
8. Veiga, A., et al., *Tackling current production of HAp and HAp-driven biomaterials.* Materials Advances, 2023. **4**(22): p. 5453-5478.
9. Puigmartí-Luis, J., *Microfluidic platforms: a mainstream technology for the preparation of crystals.* Chemical Society Reviews, 2014. **43**(7): p. 2253-2271.
10. Huang, H., et al., *Generation and manipulation of hydrogel microcapsules by droplet-based microfluidics for mammalian cell culture.* Lab on a Chip, 2017. **17**(11): p. 1913-1932.
11. Marre, S. and K.F. Jensen, *Synthesis of micro and nanostructures in microfluidic systems.* Chemical Society Reviews, 2010. **39**(3): p. 1183-1202.
12. Gimondi, S., et al., *Microfluidic Devices: A Tool for Nanoparticle Synthesis and Performance Evaluation.* ACS Nano, 2023. **17**(15): p. 14205-14228.
13. Kamperman, T., et al., *Engineering 3D parallelized microfluidic droplet generators with equal flow profiles by computational fluid dynamics and stereolithographic printing.* Lab on a Chip, 2020. **20**(3): p. 490-495.
14. Vyawahare, S., A.D. Griffiths, and C.A. Merten, *Miniaturization and Parallelization of Biological and Chemical Assays in Microfluidic Devices.* Chemistry & Biology, 2010. **17**(10): p. 1052-1065.
15. Han, T., et al., *Factory-on-chip: Modularised microfluidic reactors for continuous mass production of functional materials.* Chemical Engineering Journal, 2017. **326**: p. 765-773.
16. Veiga, A., et al., *Fabrication of calcium phosphates with controlled properties using a modular oscillatory flow reactor.* Chemical Engineering Research and Design, 2022. **183**: p. 90-103.
17. Shang, L., Y. Cheng, and Y. Zhao, *Emerging Droplet Microfluidics.* Chemical Reviews, 2017. **117**(12): p. 7964-8040.
18. Galván-Chacón, V.P., et al., *Droplet microfluidics as a tool for production of bioactive calcium phosphate microparticles with controllable physicochemical properties.* Acta Biomaterialia, 2021. **128**: p. 486-501.
19. Tsachouridis, K., Y. Zhou, and A.D. Anastasiou, *Comparison of three droplet microreactors for the continuous production of nano and micro particles.* Chemical Engineering Science, 2024. **293**: p. 119956.
20. Anastasiou, A.D., et al., *Sintering of calcium phosphates with a femtosecond pulsed laser for hard tissue engineering.* Materials & Design, 2016. **101**: p. 346-354.
21. Chen, H., et al., *Synthesis of Fluorapatite Nanorods and Nanowires by Direct Precipitation from Solution.* Crystal Growth & Design, 2006. **6**(6): p. 1504-1508.
22. Degen, T., et al., *The HighScore suite.* Powder Diffraction, 2014. **29**(S2): p. S13-S18.
23. Garstecki, P., H.A. Stone, and G.M. Whitesides, *Mechanism for Flow-Rate Controlled Breakup in Confined Geometries: A Route to Monodisperse Emulsions.* Physical Review Letters, 2005. **94**(16): p. 164501.
24. Garstecki, P., et al., *Formation of droplets and bubbles in a microfluidic T-junction—scaling and mechanism of break-up.* Lab on a Chip, 2006. **6**(3): p. 437-446.
25. Anastasiou, A.D., et al., *Sintering of calcium phosphates with a femtosecond pulsed laser for hard tissue engineering.* Materials and Design, 2016. **101**: p. 346-354.
26. LeGeros, R.Z., *Calcium phosphates in oral biology and medicine.* Monogr Oral Sci, 1991. **15**: p. 1-201.

Data Availability Statement

All the raw data presented in the paper will become available on zenodo after the acceptance of the paper for publication.